Original Article

# Synthesis and characterization of the atomic laminate Mn$_2$AlB$_2$

Sankalp Kota[a], Yexiao Chen[b], Jiayi Wang[a], Steven J. May[a], Miladin Radovic[b], Michel W. Barsoum[a],*

[a] Drexel University, Department of Materials Science & Engineering, Philadelphia, PA, USA
[b] Texas A&M University, Department of Materials Science & Engineering, College Station, TX, USA

ARTICLE INFO

ABSTRACT

Herein, we synthesize dense, predominantly single-phase polycrystalline samples of the Mn$_2$AlB$_2$ ternary compound, using reactive hot-pressing of manganese, aluminum, and boron powder mixtures under vacuum. With a Vickers hardness of 8.7 GPa, Mn$_2$AlB$_2$ is relatively soft for a transition metal boride and lacked dominant cracks at the corners of the indentations. With Young's and shear moduli of 243 GPa and 102 GPa at 300 K, respectively, it is reasonably stiff. The Poisson's ratio is calculated to be 0.19. With compressive strengths of 1.24 ± 0.1 GPa, the samples were quite strong considering the grain size (1–15 μm). The electrical resistivity at 300 K was ~5 μΩm and decreased linearly upon cooling. At 0.0036 K$^{-1}$, the temperature coefficient of resistivity was relatively high compared to MoAlB. The average linear thermal expansion coefficient was also found to be relatively high at $18.6 \times 10^{-6}$ K$^{-1}$ from 298 to 1173 K. Mn$_2$AlB$_2$ was not thermally stable above ~1379 K. While Mn$_2$AlB$_2$ was not machinable with conventional tooling, intriguingly, high-speed carbide tools bits readily penetrate the surface – with no cracking or chipping for a few millimeters – before stopping.

## 1. Introduction

Recently, the ternary transition metal (M) borides, Fe$_2$AlB$_2$ and MoAlB, have garnered renewed interest due their unique magnetic and high-temperature properties, respectively. In these compounds, M—B slabs, comprised of CrB-like face-sharing BM$_6$ trigonal prisms, are interleaved by single and double layer(s) of pure Al, respectively [1–3]. The synthesis and structures of single crystals of MoAlB and Fe$_2$AlB$_2$, along with other isostructural M$_2$AlB$_2$ compounds (M = Mn, Cr) [4,5], WAlB [6], and the related Cr$_3$AlB$_4$ and Cr$_4$AlB$_6$ layered borides, were reviewed in detail by Ade and Hillebrecht, who collectively named them the 'MAB' phases [7]. This name emphasizes the atomically laminated structure of these crystals that closely resembles the ternary M$_{n+1}$AX$_n$ carbides and nitrides, or MAX phases, which contain M$_{n+1}$X$_n$ (M = transition metal; X = C, N) blocks separated by single layers of typically Group IIIA-IVA (mostly groups 13 and 14) elements [8].

Discovered in 1969, Fe$_2$AlB$_2$ (space group *Cmmm*) [2,3] exhibits a substantial magnetocaloric effect near room temperature (RT) due to a ferromagnetic-to-paramagnetic transition above temperatures around 275–320 K, rendering it a promising material for magnetic cooling [9–11]. Ensuing work showed that its magnetic properties, including the Curie temperature, are tunable when the Fe atoms were substituted by Mn or Co [12–14]. Recently, Li et al. showed that 92 vol.% pure hot-pressed Fe$_2$AlB$_2$ ceramics have high RT ultimate compressive strengths (UCS) of ~2.1 GPa, low RT electrical resistivity (2.3 μΩm), and relatively low hardness (10.2 GPa) – relative to their binary transition metal boride counterparts – and therefore share some characteristics with MoAlB [15].

We recently showed that predominantly single phase, and fully dense, MoAlB (space group *Cmcm*) [1] ceramics have a melting point > 1673 K in vacuum and inert atmospheres [16], high compressive strengths (up to 1.9 GPa at RT), and low Vickers hardness values (~10.6 GPa) [17] compared to most binary transition metal borides [18]. As far as we are aware, it remains the only transition metal boride to date that forms protective Al$_2$O$_3$ scales when oxidized in ambient air to temperatures as high as 1350 °C [17,19]. This oxidation behavior overcomes a critical limitation of transition metal borides, for use in high temperature applications in air [20].

In general, the effect of varying M on the physical properties of isostructural Fe$_2$AlB$_2$-type compounds remains poorly understood. The dependence of hardness on the transition metal in the M$_2$AlB$_2$ phases decrease as follows: Fe$_2$AlB$_2$ > Mn$_2$AlB$_2$ > Cr$_2$AlB$_2$ on single crystals [7]. For arc melted polycrystalline samples, however, the hardness order is Cr$_2$AlB$_2$ > Fe$_2$AlB$_2$ > Mn$_2$AlB$_2$ [21]. The first study on the magnetic properties of Cr$_2$AlB$_2$ and Mn$_2$AlB$_2$ powders, with significant impurities, indicated that both lack long-range magnetic order in the

---

1.8–400 K temperature range [12]. Our recent work on the magnetic properties of high-purity $Cr_2AlB_2$ and $Cr_3AlB_4$ powders showed both compounds to be paramagnetic in the 4–375 K temperature range [22].

To better understand the properties of the MAB phases, herein we investigated the bulk synthesis of $Mn_2AlB_2$ ceramics. This phase was discovered in 1966 but was incorrectly assigned to the *C222* space group [4]. It was later re-assigned it to the *Cmmm* space group [23], which makes it isostructural with other $M_2AlB_2$ MAB phases [2,3,5]. Phase diagrams at 773 K and 1073 K show that $Mn_2AlB_2$ and $Mn_5AlB_{11}$ are stable ternary compounds in the Mn-Al-B system [5,24]. Using reactive hot-pressing of Mn-Al-B mixtures, we synthesized predominantly single-phase, dense $Mn_2AlB_2$ ceramics. Their UCS and Vickers microhardness at RT, Young's and shear moduli up to 1273 K, and thermal expansion coefficients up to 1173 K were measured. We also measured the temperature dependence of the electrical resistivity in the 5–300 K temperature range. Using differential scanning calorimetry and high-temperature quenching experiments, we studied the thermal stability in $N_2$ atmospheres.

## 2. Materials and methods

### 2.1. Synthesis

Manganese (Mn, 99.3%, −325 mesh), aluminum (Al, 99.5%, −325 mesh), and boron (B, 98%, amorphous and crystalline, −325 mesh) from Alfa Aesar (Ward Hill, MA, USA) were mixed in polyethylene jars for 24 h with $ZrO_2$ milling balls. The mixed powders, with molar ratios of 2Mn + nAl + 2B (n = 1.15–1.25), were loaded into a graphite foil-lined graphite die and placed in a vacuum hot press (HP). The sample was heated to 1323 K at a rate of 500 K/h under mechanical vacuum (< 20 Pa) and simultaneously pressed to a load corresponding to a stress of 36 MPa during the last 1 h of heating to the soaking temperature of 1323 K. This temperature and pressure were held for 2 h, after which the furnace passively cooled to RT. The bonded graphite was ground off with diamond pads, before preparing samples for further characterization.

### 2.2. Characterization

X-ray diffraction (XRD) patterns were obtained on a powder diffractometer (SmartLab, Rigaku Corp., Tokyo, Japan) using Cu Kα radiation and a detector-side graphite monochromator on thin wafers cut from the bulk HPed samples. The FullProf software suite was used to perform Rietveld refinement in the 2θ = 10–100° range [25]. The accuracy of the diffractometer in determining lattice parameters and the instrumental peak-shape function parameters were found using $LaB_6$ standard (NIST 660B). A systematic shift of −0.08% was found in the lattice parameters' evaluation as compared to the $LaB_6$ standards' reported value. The Thompson-Cox-Hastings pseudo-Voigt model was used to refine the peak shape of each phase's reflections, lattice constants, scale factors, along with the diffractogram's background parameters. For the $Mn_2AlB_2$ phase, the atomic positions were also refined. The z-displacements of both the $LaB_6$ standard and the $Mn_2AlB_2$ were obtained independently. Throughout the paper, the statistical uncertainties of Rietveld-derived parameters associated with the refinement process are reported in parentheses after a given value.

Micrographs and relative elemental compositions were obtained using a scanning electron microscope (SEM, Zeiss Supra 50 VP, Carl Zeiss SMT AG, Oberkochen, Germany), equipped with an energy-dispersive X-ray spectroscope (EDS, Oxford EDS, Oxfordshire, United Kingdom). The EDS values reported represent the average and standard deviations of 10 independent measurements selected randomly from throughout a sample's cross-section. An accelerating voltage of 15 kV and 60 s dwell time were used for each EDS measurement.

The electrical resistance was measured over the 10–300 K temperature range using a Quantum Design PPMS system. Thin wafers were

cut with a high-speed diamond wheel from the hot-pressed specimens, that were further annealed at 950 °C for 8 h under Ar, ground to a smooth finish with 800 grit SiC paper, and cleaned with ethanol prior to the measurements. Gold wires were attached to the sample with conductive silver paint, in a linear 4-probe geometry. The resistance was measured on heating and cooling in the 5–300 K temperature range.

The coefficient of thermal expansion (CTE) was measured using a Thermo-mechanical Analyzer (TMA, Q400, TA Instruments, Delaware) in the 298 K–1173 K temperature range, using heating rates of 5 K $min^{-1}$, on EDM'd and coarse grinded parallelepiped (4 × 4 × 10 mm) under nitrogen ($N_2$) gas.

Thermogravimetric analysis (TGA, SDT Q600, TA Instruments, Delaware) and differential scanning calorimetry (DSC) were performed simultaneously in $N_2$ on HP-20 samples in the 298–1573 K temperature range. The heating and cooling rates were 10 K $min^{-1}$. Quenching experiments were also performed by heating the HP-20 samples in flowing Ar to 1473 K or 1323 K, holding at that temperature for 0.5–4 h, and directly quenching into RT water. The samples were mounted into epoxy and ground with SiC papers to a 1200 grit finish for XRD and SEM measurements.

Quasi-static compression testing to failure was performed using an Instron 5800R test frame. Cylindrical samples (5 mm in diameter and 12.5 mm high) were electrical discharge machined (EDM) lengthwise parallel to the HPing direction, lightly sanded to remove any EDM-deposited residue, and sprayed with a thin layer of BN prior to mechanical testing. Six samples were compressed, using SiC spacers above and below the sample, at a rate of 0.2 mm/s.

Hardness testing was conducted with a Vickers microindenter (Leco M400, Leco Corp., St. Joseph, MI, USA) under loads of 4.9 and 9.8 N and a dwell time of 15 s. Samples were mounted in epoxy and polished down to 3 μm diamond finish prior to the indentation tests. Indentation diagonals, for 9 indents at each load, were measured in the SEM and averaged. The errors reported represent the standard deviation of the calculated hardness at each load.

## 3. Results and discussion

### 3.1. Synthesis and structure

It has been well-established in the literature that excess Al is necessary to obtain high conversion of reactants into the various MAB phases [9,12,15,17,21]. Initially, 25 mol.% excess Al was chosen here, which led to formation of predominantly the $Mn_2AlB_2$ phase. The corresponding diffractogram of this sample's bulk cross-section is plotted in green in Fig. 1a. However, some undesirable Al-rich Al-Mn intermetallics, many of which have their most intense reflections in the 40–45° range, and $Al_2O_3$ were also present. The latter likely formed by the aluminothermic reduction of surface oxides on the reagent powders or pre-existing oxide on the Al powders. To decrease these impurities, the excess Al was reduced to 15 mol.%. In this case, the binary MnB (space group *Pnma*), formed as indicated by its primary (111) and (102) peaks in the blue XRD pattern in Fig. 1a. Upon increasing the excess Al to 20 mol.%, MnB formation was suppressed and an XRD pattern consistent with predominantly single-phase $Mn_2AlB_2$ is evident (red curve in Fig. 1a). Henceforth, the sample designations HP-15, HP-20 and HP-25 will be used to designate samples produced from precursors with 15, 20 and 25 mol.% excess Al, respectively. The XRD patterns of the latter two compositions were quite comparable. The characterization and analysis reported herein were carried out on the HP-20 and HP-25 samples due the similarity in their phase compositions. We note that the samples' surfaces perpendicular to HPing direction showed slight preferential orientation of the basal {0k0} planes, which is typical when layered solids are fabricated by HPing (not shown).

Rietveld refinement of the HP-20 sample's XRD pattern was conducted to quantify the amounts of phases present and calculate the lattice parameters. The experimental and calculated diffraction pattern,
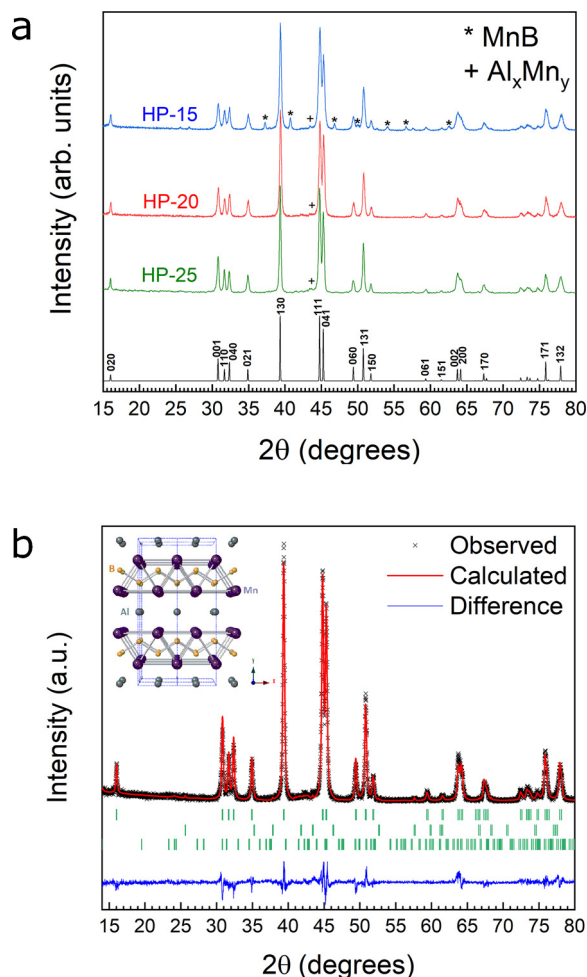
**Fig. 1.** (a) XRD patterns of bulk cross-sections after HPing at 1323 K for 2 h under 36 MPa: HP-25 (green), HP-20 (red), and HP-15 (blue). Bottom pattern (black) is the theoretical pattern (b) Rietveld refinement of a bulk cross-section of sample HP-20 showing the experimental data (black crosses), the calculated model (red curve), and Bragg positions (green markers) of $Mn_2AlB_2$ (top row), $Al_2O_3$ (middle row), and $Al_{15}Mn_{11}$ (bottom row). The refinement's $\chi^2$ value was 1.9. Inset shows crystal structure of $Mn_2AlB_2$ with Mn (purple), Al (grey), and B (yellow) (For interpretation of the references to colour in this figure legend, the reader is referred to the web version of this article).

**Table 1**

Summary of Rietveld refinement of HP-20 sample. Numbers in parentheses are estimated standard deviations (ESD) of the last significant digit obtained from the refinement process.

| Unit Cell Dimensions (Å) | 2.919(1) Å | | |
| --- | --- | --- | --- |
| | 11.060(3) Å | | |
| | 2.901(1) Å | | |
| Fit Quality | $\chi^2 = 1.85$ | | |
| | $R_{wp}$ (%) = 18.3 | | |
| Atomic Position | **x** | **y** | **z** |
| Al | 0 | 0.5 | 0.5 |
| B | 0 | 0.292(7) | 0.5 |
| Mn | 0 | 0.145(1) | 0 |
| Impurities | 5.4(4) wt.% $Al_{15}Mn_{11}$, 1.3(1) wt.% $Al_2O_3$ | | |

as shown in Fig. 1b, indicated that the sample was predominantly single-phase $Mn_2AlB_2$ along with 5.4(4) wt.% $Al_{15}Mn_{11}$ and 1.3(1) wt.% $Al_2O_3$ impurities. It is worth noting that $Al_{15}Mn_{11}$ and several other Al-rich phases of similar composition, known collectively as the γ

**Table 2**

Comparison of $Mn_2AlB_2$ lattice constants measured herein with those reported in the literature.

| Sample Type | a (Å) | b (Å) | c (Å) | Reference |
| --- | --- | --- | --- | --- |
| Single Crystals | 2.918 | 11.038 | 2.893 | [7] |
| Arc-melted | 2.923 | 11.070 | 2.899 | [21] |
| DFT | 2.895 | 11.075 | 2.831 | |
| Arc-melted | 2.936 | 11.120 | 2.912 | [12] |
| Powders | 2.92 | 11.08 | 2.89 | [4] |
| DFT | 2.887 | 11.109 | 2.83 | [26] |
| Hot-pressed | 2.919(1) | 11.060(3) | 2.901(1) | This work |

phases, are in equilibrium with $Mn_2AlB_2$ at 773 K [24]. A summary of parameters obtained from the Rietveld refinement is shown in Table 1. Since the XRD of the bulk cross-section in Fig. 1b showed no signs of texture, we did not refine for preferential orientation in the Rietveld refinement.

A summary of the lattice constants obtained herein along with those obtained from literature is shown in Table 2. The lattice constants calculated here - $a = 2.919(1)$ Å, $b = 11.060(3)$ Å, and $c = 2.901(1)$ Å - are in good agreement with values reported for $Mn_2AlB_2$ single crystals by Ade and Hillebrecht [7] and arc-melted ingots by Kádas et al. [21] Interestingly, the $b$ lattice constants reported in the literature have the greatest experimental variation. Values as high of 11.12 Å and as low as 11.038 Å, have been reported [7,12]. On the other hand, density functional theory (DFT) calculations have generally underestimated the $c$ lattice parameter by 0.06–0.07 Å compared to experimental results [21,26].

The density of HP-20 sample - measured using Archimedes' method - was 5.46 g/cm³, which corresponds to a relative density of 97.2 ± 0.2% relative to theoretical density of stoichiometric $Mn_2AlB_2$ (5.62 g/cm³). Since Fig. 2a shows an almost fully dense microstructure, the relative density measured is lower than theoretical one due to the presence of less dense intermetallics and $Al_2O_3$ impurities. From SEM images of fractured surfaces (Fig. 2b), the grain size was found to vary in the 1–15 μm range.

The backscattered electron (BSE) micrographs shown in Fig. 2a, show at least two impurity phases with different contrasts - dark grey circular grains and a non-uniformly shaped, intermediate grey phase – coexist with the $Mn_2AlB_2$ matrix. EDS revealed the former to be rich in Al and O and are thus presumed to be $Al_2O_3$ particles. The formation of $Al_2O_3$ is inevitable when starting with metal powders that have a native oxide. The non-uniformly shaped, intermediate grey phase is rich in Al and Mn and is generally located near grain boundaries and triple junctions. The EDS-measured Al:Mn atomic ratios in these regions was 2.4 ± 0.3 with small amounts of O. The Al-Mn phase diagram by McAlister and Murray [27] shows several stable phases in this compositional range (ca. 27–32 mol.% Mn), including several multi-phase fields, consisting of at least two of the following in equilibrium: $Al_{11}Mn_4$, γ, $γ_1$, $γ_2$, and liquid Al with dissolved Mn. While Rietveld refinement was consistent with the more Mn-rich $Al_{15}Mn_{11}$ phase, the fact that the most intense reflections of other Al-rich Al-Mn phases occur in the 40–45° range, makes it possible that a mixture of intermetallics, difficult to distinguish by differences in BSE contrast and XRD, exists in the samples.

Image contrast analysis of the BSE micrographs reveals the presence of 9–12 vol.% impurity phases, which agrees well with our Rietveld analysis showing around 9 vol.% (or 7 wt.%) impurities (Table 1). We note that the $Mn_2AlB_2$ grains may be slightly deficient in Al; the EDS-measured Mn:Al ratio on individual grains was 2.1 ± 0.1. Though $Mn_2AlB_2$ is assumed to be stoichiometric in the Mn-Al-B phase diagram at 773 K and 1073 K [24], Ade & Hillebrecht reported a Mn:Al ratio of 2.09 ± 0.06 for $Mn_2AlB_2$ single crystals [7]. Our numbers are thus
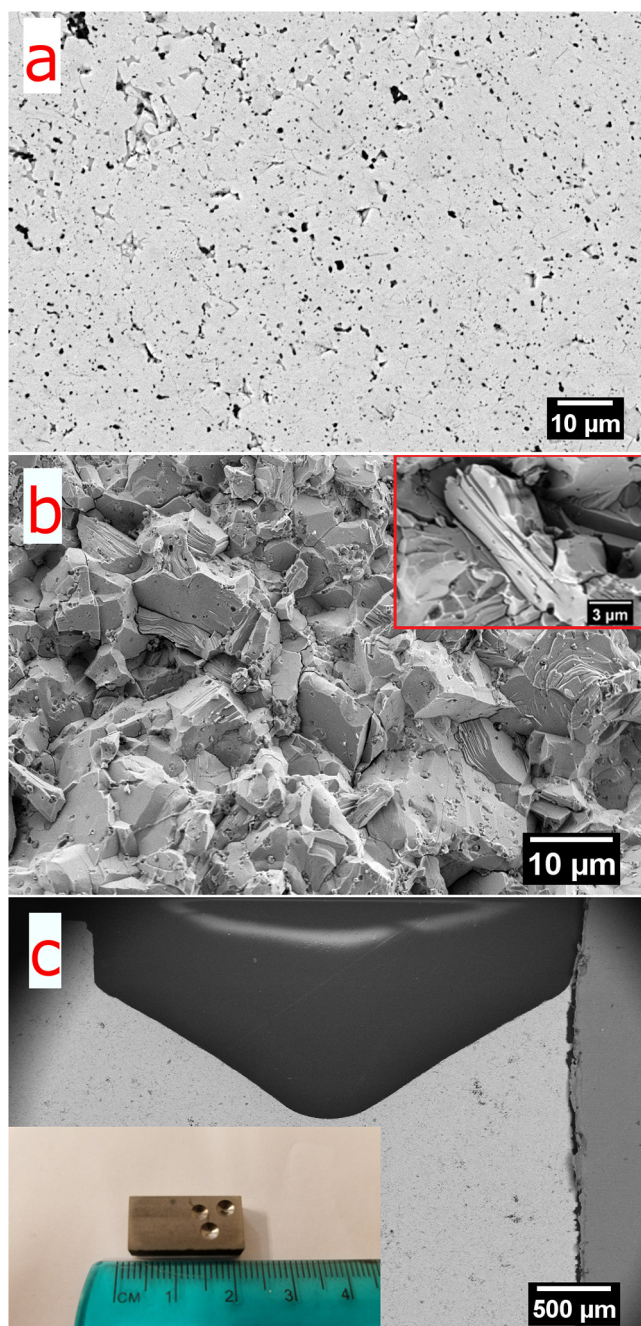
**Fig. 2.** SEM micrographs: (a) BSE image of polished cross-section of HP-20, (b) fracture surface of HP-25 cylinder compressed to failure. (c) cross-sectional SEM micrograph of drill impression made with solid carbide bits. Inset shows photograph of sample after multiple drilling attempts.



**Fig. 3.** (a) DSC/TGA in flowing $N_2$ for two cycles between RT and 1573 K on the HP-20 sample. Heat flow is shown on left y-axis; mass change on right y-axis. Inset shows the high-temperature region, (b) XRD patterns after quenching samples from 1323 K and 1473 K, (c) microstructure after quenching into water after 0.5 h annealing at 1473 K.

consistent with the latter values. SEM micrographs of fractured cross-sections are shown in Fig. 2b and are discussed in greater detail below.

### 3.2. Thermal stability

In the isothermal sections of the Mn-Al-B system, at 773 K and 1073 K, $Mn_2AlB_2$ is in equilibrium with MnB, $Mn_5AlB_{11}$, $AlB_2$, $Al_{1.67}B_{22}$, Al with Mn in solid solution, B, and several Mn-Al intermetallic phases [24]. However, $Mn_2AlB_2$ single crystals and the samples herein, have been synthesized at temperatures greater than 1323 K [7,12], which raises the question about the upper limit of this compound's thermal stability.

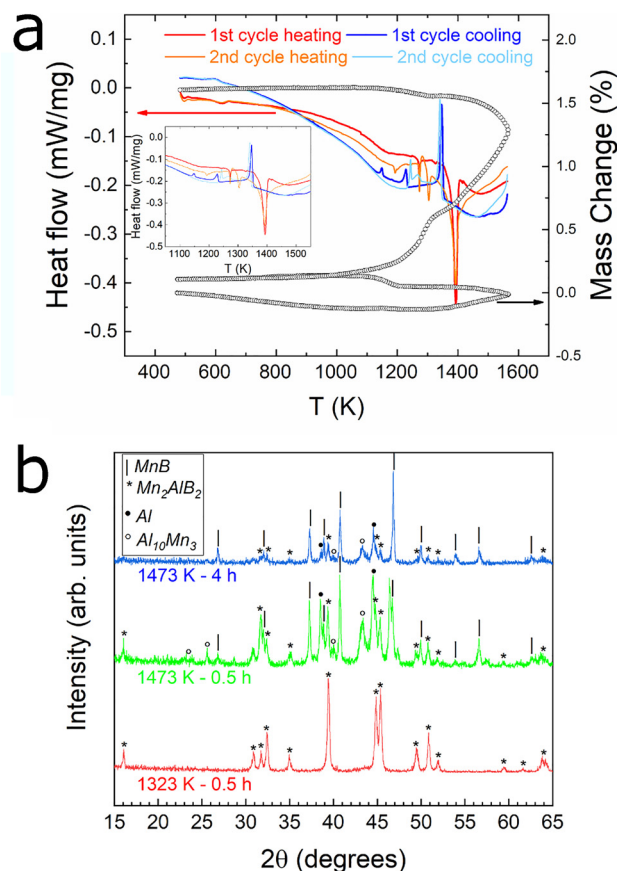The DSC/TGA results carried out on a HP-20 sample for two consecutive heating/cooling cycles, in the 298–1573 K temperature range, are shown in Fig. 3a. The first heating cycle is characterized by a small endotherm and a larger endotherm, with onset temperatures at 1269 K and 1379 K, respectively. On cooling, a large exotherm, with an onset temperature of 1353 K, and two smaller exotherms, with onsets at 1234 K and 1154 K, respectively, are observed. During the second heating cycle, the largest endotherm again has an onset temperature at 1379 K along with new, smaller endotherms with onsets at 1193 K, 1273 K, and 1305 K, respectively. During the second cooling cycle a large exotherm with onset temperature of 1346 K and two smaller ones with onsets at 1279 K and 1247 K, respectively, are observed. The small plateau that appears on both heating cycles, starting at 1170 K, may

correspond to stress relief in the sample.

The origin of large exotherm/endotherm pairs on both cycles was investigated by quenching a HP-20 sample into water from 1323 K or 1473 K, after 0.5 h soaks at those temperatures. XRD patterns after quenching from 1323 K were almost identical to those of the as-fabricated samples (compare HP-20 diffractogram in Fig. 1 with the bottommost diffractogram of Fig. 3b). On the other hand, quenching to RT after an 0.5 h soak at 1473 K, resulted in the emergence of XRD peaks belonging to MnB, Al, and $Al_{10}Mn_3$, along with those of un-decomposed $Mn_2AlB_2$. Quenching after 4 h of annealing at 1473 K, resulted in stronger MnB and $Al_{10}Mn_3$ peaks relative to those of $Mn_2AlB_2$ and Al. Note that the formation of MnB is consistent with fact that the samples quenched from 1473 K were strongly attracted to a NdFeB magnet.

Typical BSE SEM micrographs of the sample quenched from 1473 K show a fully dense microstructure with the coexistence of at least five distinct phases (Fig. 3c). EDS on areas like region 1, in Fig. 3c, suggest that this phase is MnB, with very low amounts of Al (i.e. Al:Mn and Al:B ratios < 0.1). EDS on areas like regions 2 and 3, respectively, indicate they are residual $Mn_2AlB_2$ and an intermetallic phase with an Al:Mn atomic ratio of 3.4 ± 0.2. Based on the Mn-Al phase diagram, 1473 K is above the liquidus temperature of the pre-existing γ intermetallics. Since the intermetallics found after quenching are more Al-rich and have compositions between those of $Al_4Mn$ and $Al_{11}Mn_4$ (i.e. ~21–27 at. % Mn), a mixture of these two phases, along with $Al_{10}Mn_3$, may coexist as decomposition products [28,29]. The circular grains (labelled region 4 in Fig. 3c) with darkest contrast are the pre-existing $Al_2O_3$ impurities. The dark grey phase (labelled region 5 in Fig. 3c) are rich in Al but with negligible amounts of O, suggesting they are regions of elemental Al. The EDS results are thus in good general agreement with the post-quench XRD results.

Based on the totality of these results, it is reasonable to conclude that $Mn_2AlB_2$ decomposes initially into the binary MnB and Al at temperatures > 1379 K. The small separation between the onset temperatures of the large endotherm and exotherm, and their similar peak areas, point to incongruent melting above ~1379 K. The fact that the intermetallics after quenching are more Al-rich than those in the as-

synthesized sample raises the possibility that some Al, formed initially during decomposition, reacts with the pre-existing intermetallics to form more Al-rich intermetallics, like $Al_{10}Mn_3$, found in XRD patterns after quenching. Moreover, the quenching and DSC results imply that processing temperatures much higher than 1323 K would lead to decomposition during synthesis. The decomposition of $Mn_2AlB_2$ into a binary boride is reminiscent of $Fe_2AlB_2$ into FeB + intermetallics above ~1473 K [30,31] and MoAlB into MoB + Al above ~1708 K in inert atmospheres [16]. These comments notwithstanding, it is acknowledged that more work is needed to understand the exact decomposition mechanism.

### 3.3. Elastic properties

The RT Young's (E) and shear (G) moduli, measured by RUS, were found to be 243 GPa and 102 GPa, respectively, and maintain 88% and 90% of those values at 1273 K (Fig. 4a). For reasons that are unclear, the values of E and G reported here are significantly lower than those calculated from the Voigt-Reuss-Hill approximation of DFT-predicted single-crystal elastic constants, viz. 407 GPa and 165 GPa, respectively [21]. At 300 K, the Poisson's ratio of this material is calculated, assuming ν = E/2G -1, to be 0.19, which is typical of the MAX phases [32]. The corresponding DFT-predicted value of 0.23 for $Mn_2AlB_2$ is again higher. This is unusual; typically, elastic constants predicted by DFT are within 10% of experimental results for the MAX phases [33]. It is thus reasonable to conclude that what is being modeled is not what is being measured. The fact that the DFT calculations were carried out at 0 K and assumed a perfect crystal are both contributing factors, but not enough to make up the difference. In addition, the fact that our sample contains only small amounts of impurities (9–12 vol.%) also cannot account for significantly lower elastic moduli measured herein. However, since the volume of the DFT-simulated unit cells in Ref. [21] are ~3% smaller than those found experimentally (see Table 2), the smaller equilibrium bond lengths of the former in turn would lead to overestimated DFT-calculated elastic constants. Nevertheless, more work is needed to understand the observed discrepancy. The anomalous
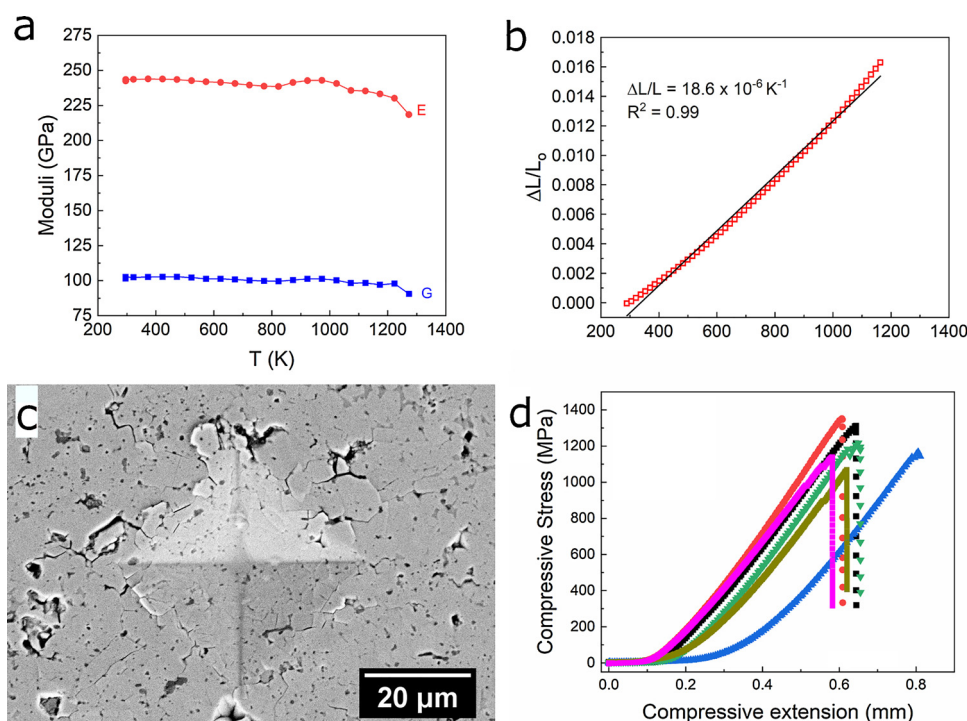


**Fig. 4.** Thermo-mechanical properties: (a) Young's and shear moduli vs. temperature (b) Relative expansion vs. temperature. (c) Typical Vickers indentation obtained at 9.8 N, (d) Stress vs. relative displacement curves for samples compressed to failure.

hump in moduli between 823–1023 K, with a maximum local increase of 2% relative to the values at 823 K, is also not understood at this time, but has been observed previously in Ni and iron-cementite alloys [34,35]. In those studies, the anomalous increase was found in the temperatures leading up to magnetic transition temperatures. Whether the same is the case in our samples is unclear and beyond the scope of this paper.

These E and G values reported here are comparable to MAX phases with the highest average number of electrons per formula unit (f.u.) such as $Cr_2AlC$ and $Cr_2GeC$. The relatively large number of electrons destabilizes the structure, as evidenced by the highest CTE and lowest G values compared to MAX phases with fewer electrons [36–38]. For example, the E and G values for $Cr_2AlC$ are, respectively, 245 GPa and 105 GPa [37].

### 3.4. Thermal expansion

The normalized thermal expansion ($\Delta L/L_o$) of a HP-20 sample up to 1173 K is shown in Fig. 4b. Approximation to a linear fit yields a relatively high CTE value of $18.6 \times 10^{-6}$ K$^{-1}$ compared to that of the paramagnetic phase of binary MnB, measured by high-temperature XRD ($11.3 \times 10^{-6}$ K$^{-1}$) [39]. Interestingly, the CTE measured herein is also considerably higher than all MAX phases measured to date, which generally have values ranging from 5 to $15 \times 10^{-6}$ K$^{-1}$, with higher values corresponding to, as alluded to above, to compositions with higher valence electron counts [40]. For example, values of $13.0–14.5 \times 10^{-6}$ K$^{-1}$ for $Cr_2GeC$ and $\approx 12.7 \times 10^{-6}$ K$^{-1}$ for $Cr_2AlC$ were reported and coincide with these compositions having the highest number of valence electrons per formula unit (f.u.). Thus, consistent with why the elastic constants are relatively low (discussed above), the CTE results also suggest that the relatively large concentration of valence electrons destabilizes the $Mn_2AlB_2$ structure. Since there are no published values on the thermal expansion of the Al-Mn intermetallic impurities, their influence on the measured CTE cannot be quantified, but they likely raised the measured value above the intrinsic value of $Mn_2AlB_2$. This assumption is reasonable when considering that, at $\sim 24 \times 10^{-6}$ K$^{-1}$ and $\sim 22 \times 10^{-6}$ K$^{-1}$, respectively, the CTE values of pure Al and Mn are significantly higher than that of the $Mn_2AlB_2$ sample.

### 3.5. Mechanical properties

The Vickers microhardness values at loads of 4.9 N and 9.8 N were $8.7 \pm 0.6$ GPa ($\sim 884$ HV) and $8.6 \pm 0.7$ GPa ($\sim 874$ HV), respectively. SEM micrographs of typical indentation marks produced under a 9.8 N load (Fig. 4c) were characterized by: (i) cracks propagating along grain boundaries around the edges of the indent, (ii) the absence of well-defined corner cracks that generally form in brittle materials and, (iii) a slight pile up of material at the indentation edges. These features, along with the weak dependence of the hardness values on the indentation load, were also observed in MoAlB [17,41] and $Fe_2AlB_2$ [15,42]. Such weak load dependences has been observed in brittle ceramics when the grain size is roughly an order of magnitude smaller than the indentation size which is the case here [43]. For example, under a 9.8 N load, the indentation diagonal is $\sim 50$ μm while the grain size is between 1–15 μm (compare Figs. 2b and 4c).

The hardness values measured herein are within the range reported for $Mn_2AlB_2$ single crystals (7.0–9.6 GPa) [7] and arc-melted samples ($7.3 \pm 0.3$ GPa) [21], but lower than those of MnB (15.7–18.2 GPa) [44,45]). Given that both $Mn_2AlB_2$ and MnB contain face-sharing $BMn_6$ trigonal prisms and B-B zig-zag chain motifs, it is reasonable to conclude that the Al layers in the ternary have a considerable softening effect. A recent DFT study predicted that ideal shear strengths along basal planes are significantly lower than those along other non-basal slip planes for the isostructural $Cr_2AlB_2$ [46]. This prediction is consistent with the nanolaminated nature of the MAB phases and thus may

also explain why the Al layers soften $Mn_2AlB_2$ relative to MnB.

These conclusions are also in line with what is known about the mechanical properties of the MAX phases [32]. However, unlike many MAX phases that can be drilled with high-speed steel bits without lubrication or cut manually with hacksaws [47], $Mn_2AlB_2$ is not readily machinable. Multiple attempts were made to drill holes into this material with solid carbide drill bits; every time the drill bit penetrated about 1–2 mm into the surface and then stopped (Fig. 2c). Removing the drill and sharpening it did not change the outcome. In other words, the outer surfaces drill readily, but not the bulk. We note in passing that MoAlB behaves similarly, and that we are currently trying to understand this intriguing phenomenon.

The RT stress vs. cross-head displacement curves for the $Mn_2AlB_2$ cylinders tested herein are shown in Fig. 4d. The mean UCS is $1.24 \pm 0.1$ GPa. Fractography on a typical failed specimen (Fig. 2b) revealed that cleavage and transgranular microcracking are both failure micromechanisms. More rarely, intragrain layer delaminations were observed (see inset in Fig. 2b), but these likely play a smaller role in failure. While the UCSs of $Mn_2AlB_2$ are quite respectable, they are not as high as those obtained on hot-pressed MoAlB ($\sim 1.4–1.9$ GPa) [17] or $Fe_2AlB_2$ ($\sim 2.1$ GPa) [15]. On the other hand, the values are higher than those of finer-grained MAX phases (grain sizes between 1–15 μm), of which only three compositions were reported to have UCS values higher than 1.2 GPa [32,48].

### 3.6. Electronic transport

The temperature dependence of the electrical resistivity (ρ) of HP-20 and HP-25 samples is shown in Fig. 5. The resistivities at 300 K ($\rho_{300}$) were $5.4 \pm 0.3$ μΩm and $5.0 \pm 0.4$ μΩm, respectively. Below 10 K, ρ is roughly independent of temperature and defect scattering leads to residual resistivities at 5 K ($\rho_5$) of 0.48–0.50 μΩm. The resulting residual resistivity ratio (RRR) – viz. $\rho_{300}/\rho_5$ – was 10.2–10.5. This RRR is relatively high for a fine-grained, polycrystalline material and implies that the samples were not too defective. Moreover, the linear increase of ρ with increasing temperature, in the 75–300 K temperature range, shows the metallic nature of $Mn_2AlB_2$. In this temperature range, the temperature dependence of resistivity can be expressed by:

$$\rho = \rho_{300}[1 + \alpha_{TCR}(T - T_o)]$$

where $T_o = 300$ K, T is the absolute temperature, and $\alpha_{TCR}$ is the temperature coefficient of resistivity. Least-square linear fittings in 75–300 K range yield $\alpha_{TCR}$ values of 0.0036 K$^{-1}$ for both samples. Together these results suggest that the slight differences in impurity phases between the HP-20 and HP-25 samples have little effect on electronic transport.
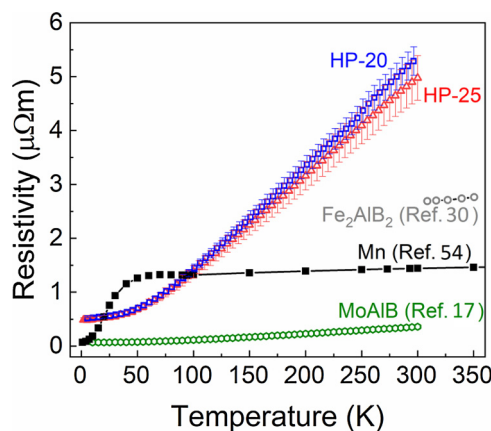


**Fig. 5.** Temperature dependence of electrical resistivity of HP-20 and HP-25 samples. The resistivities of other MAB phases and Mn metal are shown for comparison.

**Table 3**
Summary of properties measured herein for $Mn_2AlB_2$.

| Property | Value |
|---|---|
| Relative Density | $> 97.2\%$ |
| Grain Size | 1–15 μm |
| Electrical Resistivity at 300 K, $\rho_{300}$ | 5–5.4 μΩm |
| Temperature Coefficient of Resistivity, $\alpha_{TCR}$ | $0.0036\ K^{-1}$ |
| Decomposition Temperature | $\approx 1373\ K$ |
| Vickers Hardness (under 9.8 N load) | $8.7 \pm 0.6$ GPa (~884 HV) |
| Linear Thermal Expansion Coefficient (28-1173 K) | $18.6 \times 10^{-6}\ K^{-1}$ |
| Compressive Strength at RT | $1.24 \pm 0.1$ GPa |
| Young's Modulus, E (at 300 K), (at 1273 K) | 243 GPa, 219 GPa |
| Shear Modulus, G (at 300 K), (at 1273 K) | 102 GPa, 91 GPa |
| Poisson's Ratio | 0.19 |

These results confirm also that - like other transition metal borides, such as MoAlB [17] and MnB [44], among others [49–53] – electronic transport is metallic in nature. As shown in Fig. 5, our $\rho_{300}$ values are 4 times higher than Mn metal, [54] double those of $Fe_2AlB_2$ [15,30], and 13 times higher than for HPed MoAlB (0.34-0.64 μΩm at 300 K) [17,41,55]. Polycrystalline, fully dense MnB, which also contains $BM_6$ trigonal prisms, B−B zig-zag chains like $Mn_2AlB_2$ and nearly identical Mn-Mn distances, was reported to have a resistivity of 0.122 μΩm at 300 K [44]. What is most striking about these results are the exceptionally high values of $d\rho/dT$ ($\approx 1.8 \times 10^{-2}$ μΩm $K^{-1}$) compared to those of HPed MoAlB (0.0013 μΩm/K) [17] and the MAX phases (0.001–0.003 μΩm $K^{-1}$) [33]. Since $d\rho/dT$ is proportional to the electron-phonon coupling constant (λ), this result suggests that λ is quite high in this ternary. Interestingly, we did not find any results on the temperature dependence of the resistivity of MnB. Given that $\rho_{300}$ for MnB is $\approx 0.122$ μΩm [44], then the maximum value for its $d\rho/dT$ is $\approx 4 \times 10^{-4}$ μΩm/K, which is almost 50 times smaller than that of $Mn_2AlB_2$. It follows that by layering the binary boride through the introduction of Al layers, λ is enhanced by a factor of $\approx 45$.

The lower ρ reported for MnB can be related to its larger density of states at the Fermi level $N(E_f)$ compared to $Mn_2AlB_2$. For MnB, $N(E_f)$ was calculated from low temperature heat capacity measurements to be $1.35 \times 10^{23}$ $eV^{-1}$ $cm^{-3}$ [56]. While a corresponding experimental $N(E_f)$ value cannot be found in the literature for $Mn_2AlB_2$, spin-polarized DFT calculations predict a significantly lower value of $5.29 \times 10^{22}$ $eV^{-1}$ $cm^{-3}$ [26].

## 4. Conclusions

Reactive hot-pressing of Mn, Al, and B powders at 1323 K under a stress of 36 MPa resulted in dense, predominantly single-phase $Mn_2AlB_2$ polycrystalline samples, with combined ~9–12 vol.% Al-Mn and $Al_2O_3$ impurities. Above ~1379 K, in inert atmospheres, $Mn_2AlB_2$ decomposed into MnB, Al-rich Mn intermetallics, and Al. At $\approx 5$ μΩm, the RT resistivity is roughly 4 and 14 times higher than Mn metal and MnB, respectively. Moreover, a high $d\rho/dT$ of 0.018 μΩm $K^{-1}$ relative to MoAlB and the MAX phases was found and could be the related to a destabilized lattice from high valence electron count per f.u.

At ~1.2 GPa, the UCS values are quite high and exceed those of most MAX phases with similar grain sizes, viz. between 1–15 μm. At $\approx 8.7$ GPa, the Vickers hardness values are significantly lower than those of MnB, and the indentation mark lacked dominant cracks emerging from the corners, suggesting good damage tolerance. The bulk CTE was found to be $18.6 \times 10^{-6}$ $K^{-1}$ up to 1173 K. E and G were found to be 243 and 102 GPa, respectively, at RT and were very weakly T dependent up to 1273 K. The properties measured herein are summarized in Table 3.

## Acknowledgements

## References

[1] W. Jeitschko, Die Kristallstruktur von MoAlB, Monatshefte Für Chemie Und Verwandte Teile Anderer Wissenschaften 97 (1966) 1472–1476.

[2] W. Jeitschko, The crystal structure of $Fe_2AlB_2$, Acta Crystallogr. Sect. B Struct. Crystallogr. Cryst. Chem. 25 (1969) 163–165.

[3] Y.B. Kuz'ma, N.F. Chaban, Crystal structure of the compound $Fe_2AlB_2$, From Izv. Akad. Nauk SSSR, Neorg. Mater. 5 (1969) 384–385.

[4] H.J. Becher, K. Krogmann, E. Peisker, Über das ternäre Borid $Mn_2AlB_2$, Zeitschrift Fur Anorg. Und Allg. Chemie 344 (1966) 140–147.

[5] N.F. Chaban, I.U.B. Kuz'ma, Ternary systems Cr-Al-B and Mn-Al-B, Neorg. Mater. 9 (1973) 1908–1911.

[6] Y. Zhang, S. Okada, T. Atoda, T. Yamabe, I. Yasumori, Synthesis of new compound WAlB using aluminum flux, J. Ceram. Ind. Assoc. 95 (1987) 374–380.

[7] M. Ade, H. Hillebrecht, Ternary borides $Cr_2AlB_2$, $Cr_3AlB_4$, and $Cr_4AlB_6$: the first members of the series $(CrB_2)nCrA_1$ with n = 1, 2, 3 and a unifying concept for ternary borides as MAB-phases, Inorg. Chem. 54 (2015) 6122–6135.

[8] M.W. Barsoum, The $M_{N+1}AX_N$ phases: a new class of solids; thermodynamically stable nanolaminates, Prog. Solid State Chem. 28 (2000) 201–281.

[9] X. Tan, P. Chai, C.M. Thompson, M. Shatruk, Magnetocaloric effect in $AlFe_2B_2$: toward magnetic refrigerants from earth-abundant elements, J. Am. Chem. Soc. 135 (2013) 9553–9557.

[10] Q. Du, G. Chen, W. Yang, Z. Song, M. Hua, H. Du, C. Wang, S. Liu, J. Han, Y. Zhang, J. Yang, Magnetic properties of $AlFe_2B_2$ and $CeMn_2Si_2$ synthesized by melt spinning of stoichiometric compositions, J. Appl. Phys. 54 (2015), 053003.

[11] J. Cedervall, M.S. Andersson, T. Sarkar, E.K. Delczeg-Czirjak, L. Bergqvist, T.C. Hansen, P. Beran, P. Nordblad, M. Sahlberg, Magnetic structure of the magnetocaloric compound $AlFe_2B_2$, J. Alloys Compd. 664 (2016) 784–791.

[12] P. Chai, S.a. Stoian, X. Tan, P.a. Dube, M. Shatruk, Investigation of magnetic properties and electronic structure of layered-structure borides $AlT_2B_2$ (T = Fe, Mn, Cr) and $AlFe_{2-x}Mn_xB_2$, J. Solid State Chem. 224 (2015) 52–61.

[13] Q. Du, G. Chen, W. Yang, J. Wei, M. Hua, H. Du, C. Wang, S. Liu, J. Han, Y. Zhang, J. Yang, Magnetic frustration and magnetocaloric effect in $AlFe_{2-x}Mn_xB_2$ (x = 0–0.5) ribbons, J. Phys. D Appl. Phys. 48 (2015), 335001.

[14] S. Hirt, F. Yuan, Y. Mozharivskyj, H. Hillebrecht, $AlFe_{2-x}Co_xB_2$ (x = 0–0.30): $T_c$ tuning through Co substitution for a promising magnetocaloric material realized by spark plasma sintering, Inorg. Chem. 55 (2016) 9677–9684.

[15] N. Li, Y. Bai, S. Wang, Y. Zheng, F. Kong, X. Qi, R. Wang, X. He, A.I. Duff, Rapid synthesis, electrical, and mechanical properties of polycrystalline $Fe_2AlB_2$ bulk from elemental powders, J. Am. Ceram. Soc. 100 (2017) 4407–4411.

[16] S. Kota, M. Agne, E. Zapata-Solvas, O. Dezellus, D. Lopez, B. Gardiola, M. Radovic, M.W. Barsoum, Elastic properties, thermal stability, and thermodynamic parameters of MoAlB, Phys. Rev. B 95 (2017) 144108.

[17] S. Kota, E. Zapata-Solvas, A. Ly, J. Lu, O. Elkassabany, A. Huon, W.E. Lee, L. Hultman, S.J. May, M.W. Barsoum, Synthesis and characterization of an alumina forming nanolaminated boride: MoAlB, Sci. Rep. 6 (2016) 26475.

[18] G. Akopov, M.T. Yeung, R.B. Kaner, Rediscovering the crystal chemistry of borides, Adv. Mater. 29 (2017) 1604506.

[19] S. Kota, E. Zapata-Solvas, Y. Chen, M. Radovic, W.E. Lee, M.W. Barsoum, Isothermal and cyclic oxidation of MoAlB in air from 1100°C to 1400°C, J. Electrochem. Soc. 164 (2017) C930–C938.

[20] W.G. Fahrenholtz, G.E. Hilmas, Oxidation of ultra-high temperature transition metal diboride ceramics, Int. Mater. Rev. 57 (2012) 61–72.

[21] K. Kádas, D. Iuşan, J. Hellsvik, J. Cedervall, P. Berastegui, M. Sahlberg, U. Jansson, O. Eriksson, $AlM_2B_2$ (M = Cr, Mn, Fe, Co, Ni): a group of nanolaminated materials, J. Phys. Condens. Matter 29 (2017) 155402.

[22] S. Kota, W. Wang, J. Lu, V. Natu, C. Opagiste, G. Ying, L. Hultman, S.J. May, M.W. Barsoum, Magnetic properties of $Cr_2AlB_2$, $Cr_3AlB_4$, and CrB powders, J. Alloys 767 (2018) 474–482.

[23] K. Cenzual, L.M. Gelato, M. Penzo, E. Parthé, Inorganic structure types with revised space groups. I, Acta Crystallogr. Sect. B 47 (1991) 433–439.

[24] Q. Ran, Al-B-Mn, Ternary Alloy Vol. 3 VCH Verlagsgesellschaft, Weinheim, Germany, 1990, pp. 184–188.

[25] J. Rodriguez-Carvajal, FULLPROF: a program for Rietveld refinement and pattern matching analysis, Satell. Meet. Powder Diffr. XV Congr. IUCr, Toulouse, 1990.

[26] L. Ke, B.N. Harmon, M.J. Kramer, Electronic structure and magnetic properties in $T_2AlB_2$ (T = Fe,Mn, Cr, Co, and Ni) and their alloys, Phys. Rev. B 95 (2017) 104427.

[27] A.J. McAlister, J.L. Murray, The (Al-Mn) aluminum-manganese system, J. Phase Equilibria 8 (1987) 438–447.

[28] Å. Jansson, A thermodynamic evaluation of the Al-Mn system, Metall. Trans. A 23 (1992) 2953–2962.

[29] V.V. Pavlyuk, T.I. Yanson, O.I. Bodak, R. Černý, R.E. Gladyshevskii, K. Yvon, J. Stepien-Damm, Structure refinement of orthorhombic $MnAl_3$, Acta Crystallogr. Sect. C Cryst. Struct. Commun. 51 (1995) 792–794.

[30] E.M. Levin, B.A. Jensen, R. Barua, B. Lejeune, A. Howard, R.W. McCallum, M.J. Kramer, L.H. Lewis, Effects of Al content and annealing on the phase formation, lattice parameters, and magnetization of $Al_xFe_2B_2$ (x = 1.0, 1.1, 1.2) alloys, Phys. Rev. Mater. 2 (2018) 034403.

[31] J. Liu, S. Li, B. Yao, J. Zhang, X. Lu, Y. Zhou, Thermal stability and thermal shock resistance of $Fe_2AlB_2$, Ceram. Int. 44 (2018) 16035–16039.

[32] M.W. Barsoum, M. Radovic, Elastic and mechanical properties of the MAX phases, Annu. Rev. Mater. Res. 41 (2011) 195–227.

[33] M.W. Barsoum, MAX Phases Properties of Machinable Ternary Carbides and Nitrides, 1st ed., Wiley-VCH Verlag GmbH & Co, Weinheim, Germany, 2013.

[34] J. Zacharias, The temperature dependence of Young's Modulus for nickel, Phys. Rev. 44 (1933) 116.

[35] A. Kagawa, T. Okamoto, H. Matsumoto, Young's modulus and thermal expansion of pure iron-cementite alloy castings, Acta Metall. 35 (1987) 797–803.

[36] S. Amini, A. Zhou, S. Gupta, A. DeVillier, P. Finkel, M.W. Barsoum, Synthesis and elastic and mechanical properties of $Cr_2GeC$, J. Mater. Res. 23 (2008) 2157–2165.

[37] J. Hettinger, S. Lofland, P. Finkel, T. Meehan, J. Palma, K. Harrell, S. Gupta, A. Ganguly, T. El-Raghy, M. Barsoum, Electrical transport, thermal transport, and elastic properties of $M_2AlC$ (M = Ti, Cr, Nb, and V), Phys. Rev. B 72 (2005), 115120.

[38] T.H. Scabarozi, S. Amini, O. Leaffer, A. Ganguly, S. Gupta, W. Tambussi, S. Clipper, J.E. Spanier, M.W. Barsoum, J.D. Hettinger, S.E. Lofland, Thermal expansion of select $M_{n+1}AX_n$ (M = early transition metal, A = A group element, X = C or N) phases measured by high temperature x-ray diffraction and dilatometry, J. Appl. Phys. 105 (2009) 013543.

[39] T. Kanaizuka, Invar like properties of transition metal monoborides $Mn_{1-x}Cr_xB$ and $Mn_{1-x}Fe_xB$, Mater. Res. Bull. 16 (1981) 1601–1608.

[40] M.W. Barsoum, Thermal properties, MAX Phases Prop. Mach. Ternary Carbides Nitrides, 1st ed., Wiley-VCH, 2013, pp. 107–115.

[41] L. Xu, O. Shi, C. Liu, D. Zhu, S. Grasso, C. Hu, Synthesis, microstructure and properties of MoAlB ceramics, Ceram. Int. 44 (2018) 13396–13401.

[42] J. Liu, S. Li, B. Yao, S. Hu, J. Zhang, W. Yu, Y. Zhou, Rapid synthesis and characterization of a nanolaminated $Fe_2AlB_2$ compound, J. Alloys Compd. 766 (2018) 488–497.

[43] M. Sokol, M. Halabi, S. Kalabukhov, N. Frage, Nano-structured $MgAl2O4$spinel consolidated by high pressure spark plasma sintering (HPSPS), J. Eur. Ceram. Soc. 37 (2017) 755–762.

[44] S. Ma, K. Bao, Q. Tao, P. Zhu, T. Ma, B. Liu, Y. Liu, T. Cui, Manganese mono-boride, an inexpensive room temperature ferromagnetic hard material, Sci. Rep. 7 (2017) 43759.

[45] A. Cely, L.E. Tergenius, T. Lundstrom, Microhardness measurements and phase analytical studies in the Mn-B system, J. Less-Common Met. 61 (1978) 193–198.

[46] F. Dai, Z. Feng, Y. Zhou, Easily tiltable B-Al-B linear chain: the origin of unusual mechanical properties of nanolaminated MAB phases $(CrB_2)_nCrAl$, J. Alloys Compd. 723 (2017) 462–466.

[47] Z.M. Sun, Progress in research and development on MAX phases: a family of layered ternary compounds, Int. Mater. Rev. 56 (2011) 143–166.

[48] R. Benitez, H. Gao, M. O'Neal, P. Lovelace, G. Proust, M. Radovic, Effects of microstructure on the mechanical properties of $Ti_2AlC$ in compression, Acta Mater. 143 (2018) 130–140.

[49] P.A. Kumar, A.T. Satya, P.V.S. Reddy, M. Sekar, V. Kanchana, G. Vaitheeswaran, A. Mani, S. Kalavathi, N.V.C. Shekar, Structural and low temperature transport properties of $Fe_2B$ and FeB systems at high pressure, J. Phys. Chem. Solids 109 (2017) 18–25.

[50] L. Han, S. Wang, J. Zhu, S. Han, W. Li, B. Chen, X. Wang, X. Yu, B. Liu, R. Zhang, Y. Long, J. Cheng, J. Zhang, Y. Zhao, C. Jin, Hardness, elastic, and electronic properties of chromium monoboride, Appl. Phys. Lett. 106 (2015) 9–13.

[51] L. Schoop, M. Hirschberger, J. Tao, C. Felser, N.P. Ong, R.J. Cava, Paramagnetic to ferromagnetic phase transition in lightly Fe-doped $Cr_2B$, Phys. Rev. B 89 (2014) 1–7.

[52] A. Bauer, A. Regnat, C.G.F. Blum, S. Gottlieb-Schönmeyer, B. Pedersen, M. Meven, S. Wurmehl, J. Kuneš, C. Pfleiderer, Low-temperature properties of single-crystal $CrB_2$, Phys. Rev. B 90 (2014) 064414.

[53] H.J. Juretschke, R. Steinitz, Hall effect and electrical conductivity of transition-metal diborides, J. Phys. Chem. Solids 4 (1958) 118–127.

[54] P.D. Desai, H.M. James, C.Y. Ho, Electrical resistivity of aluminum and manganese, J. Phys. Chem. Ref. Data 13 (1984) 1131–1172.

[55] S. Okada, K. Iizumi, K. Kudaka, K. Kudou, M. Miyamoto, Y. Yu, T. Lundström, Single crystal growth of $(Mo_xCr_{1-x})AlB$ and $(Mo_xW_{1-x})AlB$ by metal Al solutions and properties of the crystals, J. Solid State Chem. 133 (1997) 36–43.

[56] B.D. Hanson, M. Mahnig, L.E. Toth, Low temperature heat capacities of transition metal borides, Zeitschrift Für Naturforsch. A 26 (1971) 987–991.